Gold Nanorod−pNIPAM Hybrids with Reversible Plasmon Coupling: Synthesis, Modeling, and SERS Properties

Cristina Fernández-López,[†] Lakshminarayana Polavarapu,*[,†] Diego M. Solís,[‡] José M. Taboada,[§] Fernando Obelleiro,[‡] Rafael Contreras-Cáceres,[∥] Isabel Pastoriza-Santos,*[,†] and Jorge Pérez-Juste*[,†]

[†]Departamento de Química Física, CINBIO, Universidade de Vigo and Instituto de Investigación Biomédica de Vigo (IBIV), 36310 Vigo, Spain

[‡]Departamento de Teoría de la Señal y Comunicaciones, Universidade de Vigo, 36310 Vigo, Spain

[§]Departamento Tecnología de los Computadores y de las Comunicaciones, Universidad de Extremadura, 10003 Cáceres, Spain

[∥]Departamento de Química Orgánica, Facultad de Ciencias, Universidad de Málaga, 29071 Malaga, Spain

S *Supporting Information*

ABSTRACT: The thermoresponsive optical properties of Au nanorod-doped poly(*N*-isopropylacrylamide) (Au NR−pNIPAM) microgels with different Au NR payloads and aspect ratios are presented. Since the volume phase transition of pure pNIPAM microgels is reversible, the optical response reversibility of Au NR−pNIPAM hybrids is systematically analyzed. Besides, extinction cross-section and near-field enhancement simulations for Au NR−microgel hybrids are performed using a new numerical method based on the surface integral equation method of moments formulation (M³ solver). Additionally, the Au NR−microgel hybrid systems are expected to serve as excellent broadband surface-enhanced Raman scattering (SERS) substrates due to the temperature-controlled formation of hot spots and the tunable optical properties. The optical enhancing properties related to SERS are tested with three laser lines, evidencing excitation wavelength-dependent efficiency that can be easily controlled by either the aspect ratio (length/width) of the assembled Au NR or by the Au NR payload per microgel. Finally, the SERS efficiency of the prepared Au NR−pNIPAM hybrids is found to be stable for months.

KEYWORDS: goldnanorods, thermoresponsive microgels, plasmon coupling, SERS, hot spots
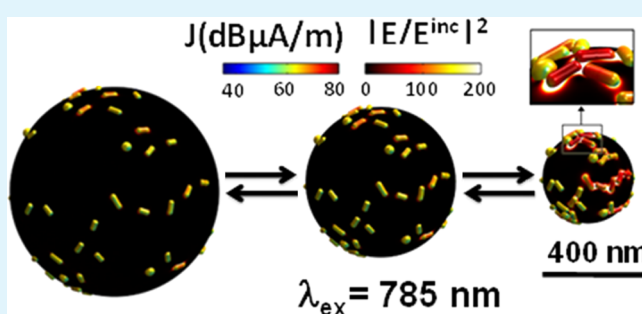
INTRODUCTION

Self-assembly of gold nanoparticles (NPs) has been a subject of interest in recent years due to the ability to create nanostructures with tailored optical properties through controlled localized surface plasmon coupling of neighboring individual Au NPs. It is of great interest in various fields such as colorimetric and surface-enhanced Raman scattering (SERS)-based sensing, electronics, and photonics.[1−5]Au NPs assemblies (random or ordered) exhibit collective plasmonic response that can be tuned from visible to near-infrared (NIR) spectrum; thus, further technological advancements of plasmonic devices depend on the ability to control their plasmon coupling through the clever design of nanoplasmonic assemblies.[1,6−10] For this reason, a large variety of methods has been developed for one-, two-, and three-dimensional (1D, 2D, and 3D) assembly of Au NPs.[11−17] These methods include assembly of NPs through chemical or physical interactions of the capping molecules,[18,19]self-assembly of NPs using polymer templates (thermosensitive and nonthermosensitive),[11,17,20−28] DNA,[29,30] carbon nanotubes,[15] graphene,[31]salts,[32,33]thiols,[34]and biorecognition.[10,35−37] Among all, DNA- and thermoresponsive polymer-templated assembly of Au NPs has been paid special

attention because of their thermosensitive reversible (assembly ↔ disassembly) nature. For example, Mirkin and co-workers have developed thermoreversible assemblies based on Au NPs that were functionalized with complementary DNA strands, and this concept was later applied for the self-assembly of anisotropic nanostructures, such as Au nanorods (NRs).[2,38] On the other hand, thermoresponsive poly(*N*-isopropylacrylamide) (pNIPAM)microgels have been used as 3D scaffolds for the assembly of Au NPs taking advantage of their responsiveness toward temperature, pH, or ionic strength.[20−27,39,40] To date, most of the reported studies so far have primarily focused on assemblies of Au or Ag spheres on microgels, but much less attention has been paid on assemblies of anisotropic NPs. Among anisotropic Au NPs, NRs exhibit rich optical properties, and their longitudinal localized surface plasmon resonance

(LSPR) could be readily tuned from visible to IR region by varying their aspect ratio (length/width); however, the SPR tunability of spherical Au or Ag NPs is limited due to their isotropic nature. For instance, Manikas et al.[25] reported the self-assembly of Au NPs physisorbed on thermoresponsive pNIPAM hydrogels exhibiting excellent SERS activity upon increasing the temperature. Very recently, Wu et al.[23] reported a shrinking strategy for creating dynamic SERS hot spots on the surface of pNIPAM microgels upon heating above its volume phase transition temperature (VPTT).

In the present work, we report the synthesis and optical properties of thermoresponsive pNIPAM microgels doped with Au NRs (Au NR–pNIPAM) with two different aspect ratios. The influence of the nanoparticle loading, as well as the temperature on the optical response of Au NR–pNIPAM hybrids, were studied by visible-NIR spectroscopy. Thus, we demonstrate that the optical properties of the Au-doped microgels can be tuned in the visible and NIR spectral region through the Au NR aspect ratio and temperature of the solution. Moreover, the optical properties and electric-field enhancements of the hybrids at both swollen and collapsed states were simulated using a numerical method (M^3 solver) based on the surface integral equation-method of moments (SIE-MOM) formulation that accurately reproduces the geometrical features of the real Au NR–pNIPAM microgels. Finally, the SERS activity of the prepared Au NR–microgel hybrids were analyzed in swollen and collapsed states for three different excitation lasers to investigate the effect of Au NR aspect ratio and loading.

■ EXPERIMENTAL SECTION

Materials. Gold(III) chloride trihydrate ($HAuCl_4 \cdot 3H_2O$), silver nitrate ($AgNO_3$), hexadecyltrimethylammonium bromide (CTAB), cetyltrimethylammonium chloride (CTAC, 25 wt % in H_2O), L-ascorbic acid (AA), hydrochloric acid (HCl), sodium borohydride ($NaBH_4$), N-isopropylacrylamide (NIPAM), N,N′-methylenebis-(acrylamide) (BIS), and allylamine were purchased from Sigma-Aldrich. Poly(vinylpyrrolidone) (PVP, MW 40 000) and potassium persulfate (KPS) were supplied by Fluka, and malachite green isothiocyanate (MGITC) was provided by Life Technologies. All chemicals were used as received. Milli-Q water with a resistivity higher than 18.2 MΩ cm was used for all the preparations.

Synthesis of Au Nanorods and Poly(vinylpyrrolidone) Coating. Au NRs with longitudinal LSPR centered at ∼610 nm and ∼730 nm (aspect ratio 2 and 3, respectively) were prepared by a previously reported seed-mediated growth method.[41,42] In a typical synthesis, a seed solution was first prepared by adding 0.6 mL of freshly prepared ice-cold $NaBH_4$ (0.01 M) solution to an aqueous mixture of 10 mL of CTAB (0.1 M) and 250 μL of $HAuCl_4$ (0.01 M) under vigorous stirring. With addition of $NaBH_4$, the solution color changed from pale yellow to brown, and the resulting seed solution was kept at room temperature for 2 h before adding into growth solution. For the preparation of shorter Au NRs (LSPR ≈ 610 nm), growth solution was prepared by adding 2 mL of $HAuCl_4$ (0.01 M), 0.1 mL of $AgNO_3$ (0.01 M), 0.32 mL of AA (0.1 M), and 0.8 mL of HCl (1.0 M), sequentially. Then 96 μL of the seed solution was added to the growth solution, which was kept undisturbed at 27 °C for 6 h to complete the growth. The synthesis of longer Au NRs (LSPR ≈ 730 nm) was performed in a similar way, but varying the amount of $AgNO_3$ added (0.3 mL of 0.01 M). The prepared Au NRs were purified by centrifugation at 8000 rpm for 30 min and redispersed in the same volume of water with a final Au concentration of 0.5 mM. This process was repeated twice. After that an aqueous PVP solution (40 mL of ∼0.5 mM, prepared by sonication for 15 min) was added dropwise to 40 mL of Au colloids under vigorous stirring. In the final mixture the molar ratio of PVP to Au metal was 1. After this mixture

was gently stirred overnight, the excess PVP was removed by centrifugation at 8000 rpm for 30 min and then redispersed in ethanol. The final Au concentration was 0.83 mM.

Synthesis of Poly(N-isopropylacrylamide) Microgels. N-isopropylacrylamide (1 g) and 0.04 g of BIS were dissolved in 50 mL of water under stirring in a three-neck flask equipped with a reflux condenser. The solution was kept under nitrogen atmosphere to remove oxygen and heated to 80 °C. Then 70 μL of allylamine and 1 mL of KPS aqueous solution (0.025g/mL) were sequentially added under stirring. The reaction was allowed to proceed at 80 °C for 2 h, after which the mixture was cooled to room temperature. To remove unreacted monomers and linear polymers the dispersion was centrifuged (30 min at 4000 rpm and 40 °C) and redispersed in the same volume of water. The process was repeated a further two times, and finally the microgels were redispersed in water.

Assembly of Gold Nanorods on Poly(N-isopropylacryla-mide) Microgels. PVP-coated gold nanorods (2.4 mL; [Au] = 0.83 mM) in ethanol were added to 12 mL of an aqueous microgel dispersion (0.24 mg/mL). It was allowed to react for 15 min under stirring, and then the mixture was centrifuged twice at 7000 rpm for 30 min and redispersed in 12 mL of water. To tune the amount of Au nanoparticles onto the microgels, further additions of Au NRs were performed. Thus, samples with four, six, and eight additions were fabricated. The average number of Au NR per microgel was estimated by transmission electron microscopy (TEM) counting the number of particles in each image and dividing that number by the number of microgels.

Synthesis of Gold Nanospheres. Citrate-stabilized Au nano-spheres of ∼55 nm in diameter were prepared by the kinetically controlled seed-mediated growth method reported by Bastus et al.[43] Briefly, 150 mL of 2.2 mM trisodium citrate aqueous solution was heated to boiling while being vigorously stirred. After 15 min, 1 mL of 25 mM $HAuCl_4$ was injected into the boiling reaction mixture, and after 10 min, the reaction mixture was cooled to 90 °C. Subsequently, 1 mL of a 25 mM $HAuCl_4$ aqueous solution was injected into the reaction mixture, and after 30 min, 1 mL of the same solution was injected again. After additional 30 min, 55 mL of the sample was extracted, and 53 mL of water and 2.2 mL of 60 mM sodium citrate was added. The final solution was then used as a seed solution, and the process was repeated (but with just two injections of the $HAuCl_4$ aqueous solution) again fivefold to yield 55 nm Au NPs. Finally, Au particles were centrifuged at 4000 rpm for 20 min and redispersed in water. The final Au concentration was 0.8 mM.

Assembly of gold nanospheres on pNIPAM microgels: 2.4 mL of as-prepared ∼55 nm gold nanospheres were added to 12 mL of an aqueous microgel dispersion (0.24 mg/mL). It was allowed to react for 15 min under stirring, and then the mixture was centrifuged twice at 6000 rpm for 20 min and finally redispersed in 12 mL of water. To tune the amount of Au nanoparticles onto the microgels, further additions of Au nanospheres were performed.

■ CHARACTERIZATION

Temperature-Dependent Optical Properties, Trans-mission Electron Microscipy, and Dynamic Light Scattering Measurements. The optical properties (visible–NIR extinction spectra) of prepared Au nanoparticles and Au NP-pNIPAM microgels were obtained with Agilent 8453 spectrophotometer. To obtain the visible–NIR extinction spectra of Au NP-pNIPAM microgels in collapsed state, the hybrids were heated in water bath at 50 °C, and their spectra were measured immediately after heating. TEM analysis was performed by using a JEOL JEM1010 transmission electron microscope operating at an acceleration voltage of 100 kV. For TEM analysis of microgels, the samples were prepared in two different ways, either by pipetting a small drop of colloids onto a TEM grid located on parafilm or by pipetting several drops of colloids onto a TEM grid located on a piece of filter paper. The average number of NRs or NPs per particle were calculated by
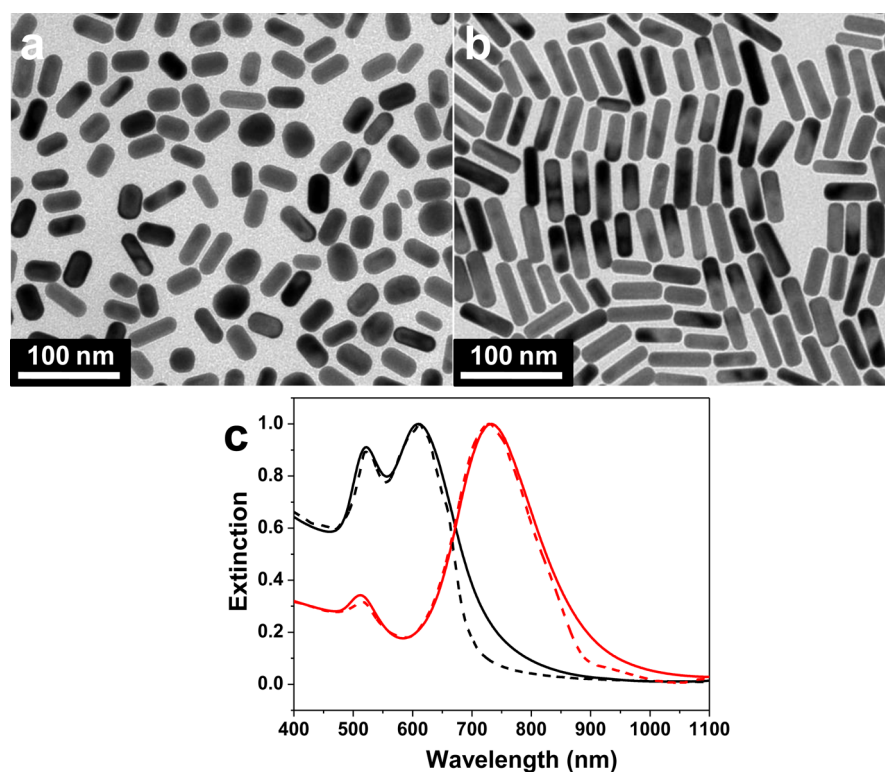
Figure 1. (a) TEM image of Au NRs with aspect ratio of 2.0 ± 0.5 and longitudinal LSPR at 610 nm. (b) TEM image of Au NRs with aspect ratio of 3.0 ± 0.6 and longitudinal LSPR at 730 nm.(c) Corresponding normalized extinction spectra of the Au NRs in water (black line, aspect ratio of 2.0 ± 0.5 and red line, aspect ratio of 3.0 ± 0.6). The continuous and dashed lines correspond to the experimental and simulated data, respectively.

averaging the number of particles and the number of microgel particles on several TEM images. Zeta potential was obtained through electrophoretic mobility measurements using a ZetasizerNano S (Malvern Instruments, Malvern U.K.) equipped with 4 mW He−Ne laser operating at a wavelength of 633 nm. Photon correlation spectroscopy (PCS) was carried out on a ZetasizerNano S (Malvern Instruments, Malvern U.K.) using a detection angle of 173.8°. The intensity-averaged particle diameter and the polydispersity index values (an estimate of the distribution width) were calculated from cumulant-type analysis. Each value was averaged from three independent measurements and after at least 5 min of equilibration time.

Surface-Enhanced Raman Scattering Measurements. At first, 1 mL of as-prepared Au NPs−pNIPAM hybrids were incubated with MGITC of final concentration of 1×10^{-6} M for 1 h, and then the average SERS signals at room temperature and at 50 °C were recorded from the composite suspensions using a micro-Renishaw InVia Reflex system equipped with Peltier charge-coupled device (CCD) detector and three excitation laser lines (633, 785, and 830 nm). To measure the SERS signals at 50 °C, the samples were kept in water bath at 50 °C until thermal equilibrium was achieved, and then the SERS signals were collected. The Raman spectra of MGITC was obtained from a film made by drop-casting a 20 μL aliquot of 1×10^{-3} M MGITC solution on glass followed by air drying. The average SERS enhancement factors at 785 and 830 nm excitations were determined by comparing the signals acquired from MGITC solution at a concentration 0.5 mM with SERS signals obtained from 1 μM MG solution with Au NR−microgel hybrid colloids (prepared by six additions of Au NRs, aspect ratio of 2). The average enhancement factors (EFs) were

calculated using the formula EF = $(I_{SERS}/I_{ref})(C_{ref}/C_{SERS})$.[44,45] However, the EF at 633 nm excitation is difficult to determine due to strong fluorescence background from MGITC.

Numerical Simulations. Extinction spectra and near-field enhancement simulations for Au NR−pNIPAM hybrids were obtained using a numerical method based on the SIE-MOM formulation (M^3 solver).[46] In this method, we consider a model consisting of a sphere made of dielectric media representing pNIPAM microgels with gold nanorods randomly distributed on its surface with dimensions estimated from the experimental results (dynamic light scattering (DLS) for the pNIPAM microgels and TEM for Au NRs), with water being the solvent (see Figure 5b). The metallic nanostructures were replaced by equivalent electric and magnetic currents placed over the particle boundary surfaces and interfaces. We derive a set of SIE values for the unknown equivalent currents through the integro-differential Stratton−Chu representation formulas and the boundary conditions for the total fields. These SIEs were subsequently discretized by applying a Galerkin MOM procedure in terms of a set of basis and testing functions, leading to a dense $N \times N$ matrix system of linear equations (N being the number of basis functions used to expand the unknown equivalent currents). For the realistic simulation of the large-scale plasmonic systems considered here, SIE-MOM was expedited via the multilevel fast multipole algorithm-fast Fourier transform (MLFMA-FFT),[47] providing a high algorithmic efficiency—computational cost of O(NlogN)—along with high-scalability via parallelization using multicore computer clusters. The simulations were executed with a work-station mounting 4 Intel Xeon E7−8880v2 microprocessors, each with 15 cores clocked at 2.50 GHz, which gives as 60 physical processors overall (no hyper threading is used).
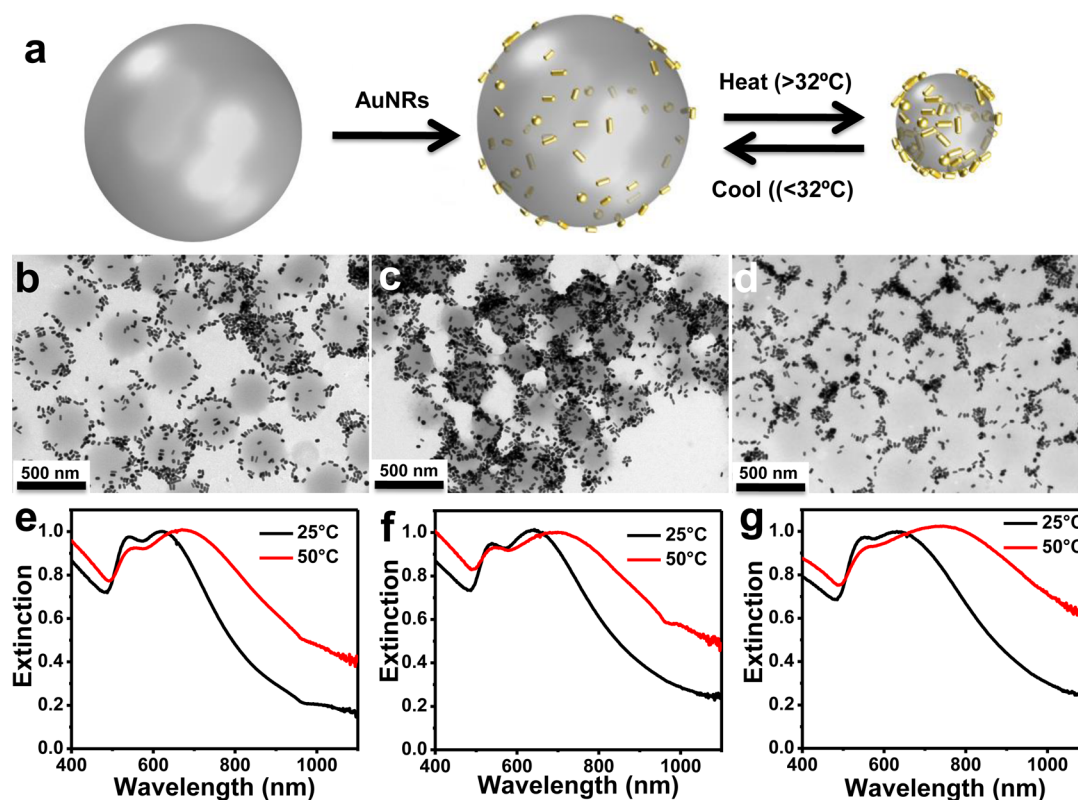
Figure 2. (a) Schematic representation of the Au NR−pNIPAM hybrid synthesis and the corresponding thermoresponsive behavior. (b−d) Representative TEM images of Au NR−microgel hybrids prepared with four (b) and six (c, d) additions of Au NR (aspect ratio of ∼2). The difference between (c) and (d) is the TEM grid preparation (see main text for details). (e, f) vis−NIR normalized extinction spectra of Au NR− pNIPAM hybrids at 25 °C (black line) and 50 °C (red line) with four (e), six (f), and eight (g) Au additions.

Approximately 163 000 unknowns per particle were considered to model both the Au NRs and the microgel sphere, requiring ∼12 GB of memory and 2050 s of execution time per wavelength and per particle (while all orientations are calculated at a time). The dielectric data for Au were taken from Johnson and Christy,[48] and the temperature-dependent refractive index of pNIPAM was taken from ref 49.

■ RESULTS AND DISCUSSION

To analyze the optical response of thermoresponsive nanostructures constituted by Au NR-doped pNIPAM microgels, Au NRs of two different aspect ratios (Figure 1a,b), with well-differentiated optical features (Figure 1c), were synthesized. While TEM analysis revealed that Au nanorods presented an average aspect ratio of 2.0 ± 0.5 and 3.0 ± 0.6 (see more details in Figure S1, Supporting Information), the corresponding extinction spectra showed the characteristic spectral features from Au nanorods with the longitudinal LSPR centered at 610 nm and at 730 nm, respectively. The extinction spectra of both Au samples were modeled using a numerical method based on the SIE-MOM formulation (see Experimental Section for details). We considered a model consisting of cylinder with hemispherical end cups (for the Au NRs) and a sphere (for the Au spheres) and the size distribution histograms of Au NRs and the percentage of spherical NPs obtained from TEM analysis. As shown in Figure 1c calculations of the extinction cross-section show a good agreement with the experimental observations for both samples. On the other hand, pNIPAM microgels with average hydrodynamic diameters of 770 ± 17 nm at 25 °C and 278 ± 4 nm at 50 °C, and a volume phase

transition temperature of ca. 32 °C (see Figure S2 in the Supporting Information), were synthesized via copolymerization of NIPAM and allylamine in the presence of BIS as cross-linker (nominal 3%, see Experimental Section for details).

The synthesis of Au NR−pNIPAM nanostructures was performed through the layer by layer technique. pNIPAM microgels were positively charged particles (zeta potential = +13.1 ± 1.0 mV at 25 °C and +29.3 ± 1.2 mV at 50 °C), and the as-prepared Au NRs also presented a positive surface charge because of the CTAB bilayer adsorbed onto their surface. Therefore, to electrostatically attach the Au NRs onto the microgel surface, they were coated with PVP to confer on them a slightly negative charge (−20 mV).[50] Next, negatively charged PVP-modified Au NRs were loaded onto positively charged microgels by adding Au NR solution to microgel colloids under continuous stirring, followed by centrifugation to remove unbound Au NRs (see Figure 2). The number of NRs per microgel colloid was easily tuned through sequential additions from the Au NR stock solution. Thus, an average of 25, 60, and 85 Au NR per microgel was determined for four, six, and eight additions, respectively (as revealed the TEM analysis). Figure 2b,c shows representative TEM images of the hybrid composites with four and six additions of Au NRs with an average aspect ratio of ∼2.0. Although in certain regions the particles appeared to be aggregated and not homogeneously distributed, it can be attributed to a drying effect on the TEM grids. In fact, if the TEM grid was prepared by placing the grid on a piece of filter paper to rapidly wick away the solvent (see Experimental Section for details) the Au NR tended to be
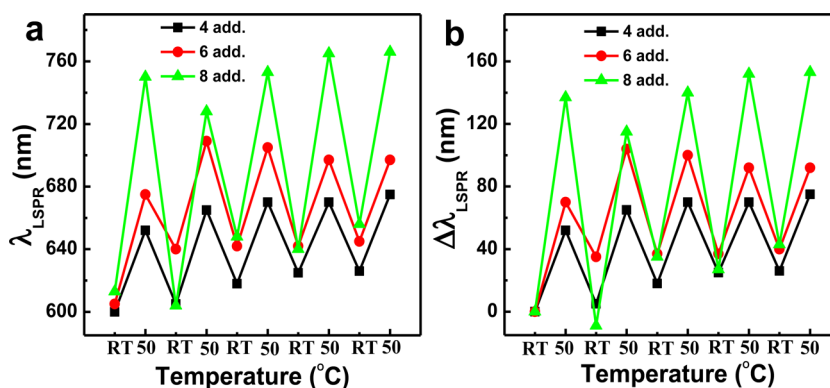
Figure 3. (a) Variation of longitudinal LSPR maxima and (b) the corresponding LSPR shift of Au NR−microgel hybrids at 25 °C (swollen state) and 50 °C (collapsed state) for different cycles.

arranged at the sides of the microgels in a sort of hexagonal packing (see Figure 2d).

The optical properties of the thermoresponsive Au NR−pNIPAM hybrids were studied by visible−NIR absorption spectroscopy at the swollen (25 °C) and collapsed (50 °C) states. Furthermore, for a better understanding of the Au NR loading effect in the optical properties samples with four, six, and eight additions were analyzed (Figure 2e−g). At 25 °C the Au NR−pNIPAM hybrids with the different number of NP loadings showed similar spectral features, two LSPR bands located at ∼540 and 630 nm, which allowed us to consider weak electronic interactions among nanorods. On the contrary, the hybrids displayed different optical responses in comparison to the ones from Au NR dispersions (see Figure 1c). Thus, the plasmon bands shifted to red and broadened when the Au NRs were deposited on microgels, which can be ascribed to the large scattering contribution of microgels at low wavelengths, the increase in the local refractive index near the Au NR, and weak plasmon coupling effects. In addition, it was found that the LSPR band broadened even at room temperature with increasing the number of Au NRs per particle. It can be explained in terms of coupling effect, which got more intense with the number of Au NRsper microgel.

The spectra recorded at 50 °C (collapsed state) showed changes mainly on the longitudinal LSPR band, namely, a red shift and a broadening of the band (see Figure 2e−g). These effects were readily interpreted in terms of a decrease in the interparticle distance upon reduction of the particle volume when the microgel collapsed, causing strong plasmon coupling. These interactions have been classified into tip-to-tip, tip-to-side, and side-to-side interactions,[26] the first two being more probable and also stronger than the latter and resulting in both cases in a red shift. Furthermore, the extension of the red shift with the microgel collapse relied on the Au NR loading. An increase in the average Au NR per microgel from 25 to 85 (increase in Au NR addition from 4 to 8) led to an increase in the red shift from 50 to 140 nm of the longitudinal plasmon band, as well as a band broadening upon microgel collapse.

Since the volume phase transition of pNIPAM microgel is reversible,[26] the thermoresponsive optical behavior of the Au NR−pNIPAM hybrids were expected to be reversible too, unless aggregation of rods takes place in the collapsed state. The confirmation of this reversible optical response is shown in Figure 3, where the position of the longitudinal LSPR band was plotted as a function of the swelling and collapse events. It clearly indicated that the original distribution of rods onto the

microgels were recovered after each cycle. We further analyzed the influence of Au NR aspect ratio on the optical properties of hybrids using Au NRs with an average aspect ratio of 3.0 ± 0.6 and therefore the longitudinal LSPR centered at 730 nm (see Figure 1). The TEM characterization of the Au NR−pNIPAM microgels revealed a relatively homogeneous distribution of the particles around the microgels (see Figure 4a). The visible−
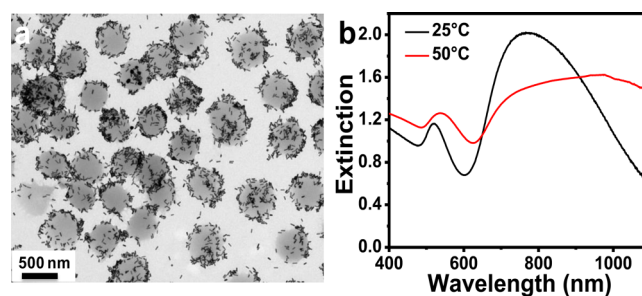

Figure 4. (a) Representative TEM image of Au NR−pNIPAMhybridssynthesized using Au NRs with aspect ratio of 3.0 ± 0.6. (b) Corresponding visible−NIR extinction spectra of hybrids at 25 °C (black) and 50 °C (red).

NIR spectra of hybrids at 25 °C (swollen state) and 50 °C (collapsed state) showed red shift and broadening of the Au NR longitudinal LSPR (see Figure 4b). Interestingly, since the swollen Au NR−pNIPAM microgels displayed the longitudinal LSPR around 770 nm, the extinction spectra of collapsed hybrid microgels red-shifted into the NIR region (ca. 950 nm). Therefore, the careful control of the Au NR aspect ratio and the Au loading onto the microgel should allow control of the optical properties of the hybrids.

To understand and correlate the Au NR distribution on the microgels upon loading with their optical properties, the extinction spectra of the Au NR−pNIPAM hybrids with six additions of Au NRs (aspect ratio of ∼2) were simulated. Although conventional simulation methods (e.g., FDTD, DDA, BEM) could be utilized for the calculations, they require large calculation costs to provide reliable optical information about such complex objects. So, we employed a recently reported methodology,[46,47] which implements accelerated calculations based on SIEs with the method of moments (MOM)[51] formulation and the multilevel fast multipole algorithm.[52,53] The SIE-MOM approach expedited via MLFMA brings some unique advantages with respect to volumetric approaches, such as lower computational cost (as only the particle boundaries
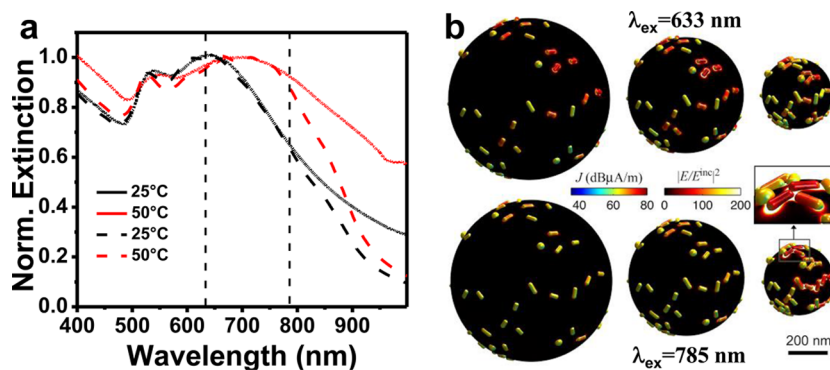
Figure 5. (a) Experimental (solid lines) and simulated (dashed lines) extinction spectra of hybrid colloids (prepared by six additions of Au NRs, aspect ratio of 2) at 25 °C (black) and 50 °C (red). (b) Simulation of surface electric current on individual Au NRs (J(dB μA/m)) and electric near-field intensity enhancements ($|E/E^{inc}|^2$) caused by plasmon coupling of Au NRs on microgel colloids at 633 and 785 nm and with different extents of shrinking.

and interfaces must be parametrized) and larger stability, particularly when dealing with resonant metallic response (as the singular behavior of fields is analytically handled by the Green's function and its derivatives). The computational power of this approach, which is O(N log N) both in memory and time, N being the number of basic functions (unknowns) to represent the surface electric and magnetic equivalent currents, allowed us to model the particles in their full complexity. To simulate the optical properties of the Au NR–pNIPAM hybrids we considered a model consisting of a sphere made of dielectric media representing pNIPAM microgels with hemispherical-capped cylinders of gold randomly distributed on its surface. The average number of Au NRs per microgel was estimated from the TEM images (average number of 60 Au NRs per microgel for six additions of Au NRs). Since the TEM images did not really give the exact arrangement of the Au NR on the microgel as they were obtained in dry state, we considered various possible configurations for the assembly to fit both the swollen and collapsed states. In all cases, randomly oriented Au NRs with different dimensions according to the size distribution histograms obtained by TEM (see Supporting Information, Figure S1) were considered. Bearing this in mind, we simulated the spectra of 60 Au NRs randomly distributed on a pNIPAM microgel considering 20 different configurations/arrangements, and with 12 different incident angles for the incoming light. Thus, the obtained extinction spectrum was the result of averaging 240 spectra. Besides the simulations were carried out by considering 163 000 unknowns per particle to model both the Au NRs and the microgel sphere as described in detail in Experimental Section. As shown in Figure 5a, the numerically calculated spectra for both swollen and collapsed states were in strikingly good agreement with the experimental observations. To further visualize the plasmon coupling with respect to the decrease of microgel size, we calculated the surface electric current (J(dB μA/m)) on the Au NRs arranged on a hybrid system for different extents of microgel shrinking and the respective electric near-field intensity enhancements ($|E/E^{inc}|^2$) at two different wavelengths (633 and 785 nm) as shown in Figure 5b. In the total swollen state (at lower temperatures) the surface current on Au NRs at 633 nm was higher than at 785 nm as it matched with the LSPR band when no coupling between particles were presented. However, in the collapsed state the electric field enhancement was higher at 785 nm than at 633 nm as the plasmon coupling led to a LSPR red shift. A movie representing the reversible transformation of

swollen and collapsed states with their field enhancements at 785 nm is provided in the Supporting Information. It clearly shows that the Au NR–pNIPAM hybrids exhibit strong coupling in the NIR region in collapsed state. In addition, the optical properties of Au NR–microgel hybrids prepared by eight additions of Au NRs (85 NRs per microgel) were also simulated at both 25 and 50 °C, and they are in good agreement with experimental spectra (Figure S3 in the Supporting Information). The increase in the density of NRs per microgel leads to strong interparticle plasmon coupling, which results in the LSPR peak broadening and red shift at both temperatures.

We have shown, so far, that by controlling the aspect ratio of Au NR and microgel loading it was possible to obtain Au NR–pNIPAM hybrids with widely tunable optical properties and a reversible thermosensitive plasmon coupling. Although the SERS properties of Au and Ag NPs loaded onto thermoresponsive microgel hybrids have been investigated recently, most of the reported SERS studies were performed on isotropic Au or Ag NP assemblies on microgel colloids.[24,25] Moreover, excitation wavelength-dependent SERS studies on such hybrids have not been investigated in detail. It is well-known that excitation wavelength has a large influence on SERS activity.[54–57] So, it would be interesting to study how the reversible thermoresponsive plasmon coupling (collapsed and swollen states of hybrid) influences the excitation wavelength-dependent SERS activity of Au NR–microgel hybrids.

The SERRS and SERS properties of the different Au NR–pNIPAM hybrid microgels (four and six additions of Au NRs with aspect ratio 2; see Figure 2) were analyzed by using MGITC (1 μM) as Raman active probe with three different excitation lasers ranging from the visible (633 nm) to the NIR (785 and 830 nm). The UV–vis absorption spectra of MGITC is shown in Supporting Information (Figure S4), and it shows a strong peak 616 nm, which is close to 633 nm excitation laser lines. So,the excitation of MGITC with 633 nm laser line produce surface-enhanced resonance scattering (SERRS) signals. It was found that hybrid colloids prepared with eight additions of Au NRs tend to settle in short time due to higher density. So the SERS properties of hybrids with 85 NRs per particle were not evaluated. Figure 6a shows the SERRS (with 633 nm excitation) and SERS (with 785 and 830 nm excitations) spectra obtained for MGITC with the three laser lines using Au NR–pNIPAM hybrids with six additions. The spectra show the characteristic SERS peaks for MGITC:[58,59] in-
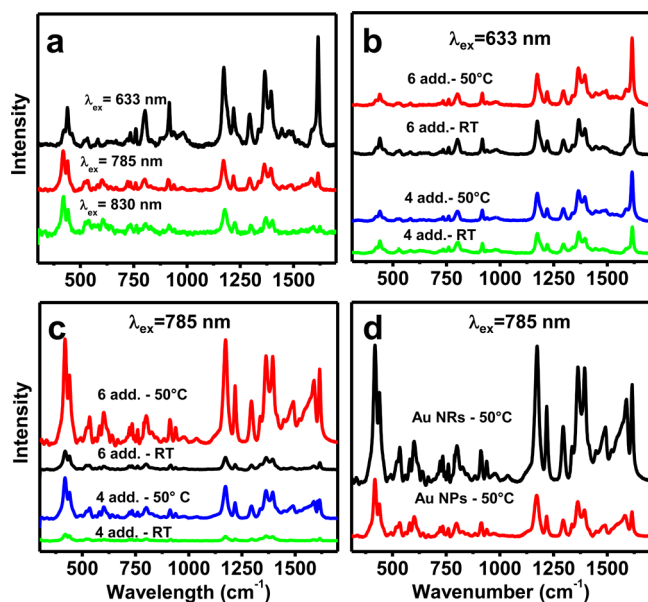
Figure 6. (a) Excitation wavelength dependent SERS spectra of MGITC in the presence of Au NR–microgel hybrids obtained with six additions of Au NRs with aspect ratio 2. (b, c) SERRS andSERS properties of Au NR–microgel hybrids (four and six Au NR additions as indicated) at both room temperature and at 50 °C with 633 nm (b) and 785 nm (c) excitation lasers. (d) SERS spectra of Au NR–microgel and Au NP-microgel hybrids using MGITC and using 785 nm excitation.

plane C–C at 1618 cm^{-1}, C–H out-of-plane bending mode at 917 cm^{-1}, C–H in-plane bending mode at 1172 cm^{-1}, in-plane phenyl ring stretch at 1584 cm^{-1}, N-phenyl stretching (1397 cm^{-1}), out-of-plane motion of the aromatic hydrogens at 803 cm^{-1} and benzene vibrations at 440 and 420 cm^{-1} (doublet). The relative intensities of several peaks varied depending on the excitation wavelengths due to surface selection rules.[54,56] For example, the peak at 1618 cm^{-1} decreased relative to 420 cm^{-1} with increasing the excitation wavelength. To understand the variation in the relative intensities of different SERS peaks with respect to excitation wavelength, the SERS spectra of MGITC with three different laser lines were compared with extinction spectra of Au NR-hybrid particles (FigureS4 in the Supporting Information). Clearly, the enhancement of different peaks varied with respect to excitation wavelength due to the variation in the coupling with extinction spectra of hybrid particles (Figure S4 in the Supporting Information). The excitation wavelength-dependent SERS spectra showed that the peak at 1618 cm^{-1} strongly couples with SPR maximum of relative to other peaks at 633 nm excitation, while it showed weak coupling at 830 nm (Figure S4 in the Supporting Information). However, the data clearly showed that the hybrids exhibited broad-band SERS activity with all three excitation lasers although the relative intensities varied depending on excitation wavelengths.

To study the effect of the reversible plasmon coupling in the SERS activity of Au NR–microgel hybrids (four and six additions of Au NRs with aspect ratio 2), the SERS spectra recorded at swollen state (25 °C) and collapsed state (50 °C) were analyzed for the three laser lines (Figure 6b,c and Figure S5 in Supporting Information). A slight increase was seen in the SERRS intensity at 633 nm excitation, while at 785 and 830 nm significant SERS enhancement was observed in collapsed state

of the Au NR–pNIPAM microgels. These results could be easily explained considering the thermosensitive optical properties exhibited by the hybrid colloids at swollen and collapsed state and displayed in Figure 2d,e. Thus, the extinction contribution at 633 nm was not altered after the microgel collapsed (there is no significant contribution from the plasmon coupling); however, at 785 and 830 nm a significant increase of the extinction contribution was observed as a result of the strong coupling between neighboring Au NRs upon collapse. Although similar thermoresponsive SERS behaviors were observed for hybrids obtained with four and six Au NRs additions, the SERS efficiency at collapsed state was higher for six additions because of the high density of hot spots. The average enhancement factors obtained for six Au NRs additions were ∼18 × 10^3 and 2.3 × 10^3 with 785 nm excitation and 16 × 10^3 and 2.8 × 10^3 with 830 nm excitation for the peaks at 420 and 1618 cm^{-1}, respectively. However, it was difficult to obtain enhancement factor with 633 nm excitation due to strong fluorescence background.

Additionally, the SERS efficiency of the Au NR–microgel hybrids prepared with Au NRs with aspect ratio of 3 (see Figure 4) was also analyzed in the swollen and the collapsed states with 785 nm laser line. As shown in Figure S6 in Supporting Information, the microgel collapse led to a decrease in the SERS intensity. The different behavior presented by these hybrids could be explained in terms of extinction contribution decrease at 785 nm as a result of the strong red shift of the main LSPR (ca. 1000 nm) upon collapse. Hybrids fabricated with 50 nm Au nanospheres that exhibited optical features (λ_{max}) at 550 (swollen state) and 580 nm (collapsed state) (see Figure S7 in Supporting Information) showed similar SERS activity with the 633 nm but lower activity with 785 and 830 nm when compared to Au NR-pNIPAM hybrids (Figure 6d and Figure S8 in Supporting Information, respectively). These results clearly support that the SERS intensity depends on the position of LSPR peak with respect to the excitation wavelength.[60]

The obtained results suggested that Au NR–microgel hybrid colloids could be useful as SERS substrates and SERS labels as they are quite stable in proper loading of Au NRs. To be applied in practical applications, the assemblies should be stable for long time, which is a major problem with nanoparticle assemblies of various kinds. To test the long-term stability of Au NR–microgel hybrids, SERS measurements were performed on freshly prepared and three months old hybrid samples, and they exhibit similar SERS activity, indicating long-term-stability (see Figure S9, in the Supporting Information).

■ CONCLUSIONS

The thermoresponsive optical properties of Au NR-doped pNIPAM microgels were studied with different Au NR payloads and aspect ratio regimes observing a fully reversible behavior. The experimental data were compared with computational results obtained by means of the M^3 surface integral-equation solver that accurately reproduces the structural features of the real hybrids. Besides, electric-field enhancements for the Au NR–pNIPAM hybrids at collapsed and swollen state were calculated with the M^3 solver. Finally, the thermoresponsive SERS activity of the hybrids was analyzed for three different laser lines, evidencing excitation wavelength-dependent efficiency that can be easily controlled by either the aspect ratio (length/width) of the assembled Au NR or by the Au NR payload per microgel. It was also found that the Au NR–

microgel hybrids exhibit higher SERS activity over Au NP−microgel hybrids with NIR excitation. The excitation wavelength-dependent and thermoresponsive SERS results clearly support the electromagnetic field-enhancement mechanism. One can design the Au NR−pNIPAM hybrids with varying Au NRs aspect ratios depending on the excitation wavelength that is needed specific applications. Overall, this study opens new room for the design and fabrication of thermosensitive polymer−metal NR hybrids to be used as efficient SERS active substrates and labels.

ASSOCIATED CONTENT

Ⓢ Supporting Information

Size distribution histograms of Au NR, TEM, and DLS characterization of the pNIPAM-co-allylamine microgels, additional numerical simulations and SERS characterization of different hybrid systems. Absorption spectra of MGITC, Raman spectra of MGITC (solid) with three laser lines, a movie representing the reversible transformation of swollen and collapsed states of a Au NR−pNIPAM hybrid with their field enhancements at 785 nm. This material is available free of charge via the Internet at http://pubs.acs.org.

AUTHOR INFORMATION

Corresponding Authors

*E-mail: lakshmi@uvigo.es. (L.P.)
*E-mail: juste@uvigo.es. (J.P.-J.)
*E-mail: pastoriza@uvigo.es. (I.P.-S.)

Notes

The authors declare no competing financial interest.

ACKNOWLEDGMENTS

REFERENCES

(1) Polavarapu, L.; Perez-Juste, J.; Xu, Q. H.; Liz-Marzan, L. M. Optical Sensing of Biological, Chemical and Ionic Species Through Aggregation of Pasmonic Nanoparticles. *J. Mater. Chem. C* **2014**, *2*, 7460−7476.

(2) Elghanian, R.; Storhoff, J. J.; Mucic, R. C.; Letsinger, R. L.; Mirkin, C. A. Selective Colorimetric Detection of Polynucleotides Based on the Distance-Dependent Optical Properties of Gold Nanoparticles. *Science* **1997**, *277*, 1078−1081.

(3) Webb, J. A.; Bardhan, R. Emerging Advances in Nanomedicine with Engineered Gold Nanostructures. *Nanoscale* **2014**, *6*, 2502−2530.

(4) Liu, D.; Wang, Z.; Jiang, X. Gold Nanoparticles for the Colorimetric and Fluorescent Detection of Ions and Small Organic Molecules. *Nanoscale* **2011**, *3*, 1421−1433.

(5) Yuan, P.; Ma, R.; Guan, Z.; Gao, N.; Xu, Q. H. Tuning Two-Photon Photoluminescence of Gold Nanoparticle Aggregates with DNA and Its Application as Turn-on Photoluminescence Probe for DNA Sequence Detection. *ACS Appl. Mater. Interfaces* **2014**, *6*, 13149−13156.

(6) Guerrero-Martínez, A.; Grzelczak, M.; Liz-Marzán, L. M. Molecular Thinking for Nanoplasmonic Design. *ACS Nano* **2012**, *6*, 3655−3662.

(7) Guerrini, L.; Graham, D. Molecularly-Mediated Assemblies of Plasmonic Nanoparticles for Surface-Enhanced Raman Spectroscopy Applications. *Chem. Soc. Rev.* **2012**, *41*, 7085−7107.

(8) Gill, R. S.; Saraf, R. F.; Kundu, S. Self-Assembly of Gold Nanoparticles on Poly(allylamine Hydrochloride) Nanofiber: A New Route to Fabricate "Necklace" as Single Electron Devices. *ACS Appl. Mater. Interfaces* **2013**, *5*, 9949−9956.

(9) Chen, M.-C.; Yang, Y.-L.; Chen, S.-W.; Li, J.-H.; Aklilu, M.; Tai, Y. Self-Assembled Monolayer Immobilized Gold Nanoparticles for Plasmonic Effects in Small Molecule Organic Photovoltaic. *ACS Appl. Mater. Interfaces* **2013**, *5*, 511−517.

(10) Tian, Z.; Yang, C.; Wang, W.; Yuan, Z. Shieldable Tumor Targeting Based on pH Responsive Self-Assembly/Disassembly of Gold Nanoparticles. *ACS Appl. Mater. Interfaces* **2014**, *6*, 17865−17876.

(11) Polavarapu, L.; Xu, Q. H. Water-Soluble Conjugated Polymer-Induced Self-Assembly of Gold Nanoparticles and Its Application to SERS. *Langmuir* **2008**, *24*, 10608−10611.

(12) Ofir, Y.; Samanta, B.; Rotello, V. M. Polymer and Biopolymer Mediated Self-Assembly of Gold Nanoparticles. *Chem. Soc. Rev.* **2008**, *37*, 1814−1825.

(13) Lin, S.; Li, M.; Dujardin, E.; Girard, C.; Mann, S. One-Dimensional Plasmon Coupling by Facile Self-Assembly of Gold Nanoparticles into Branched Chain Networks. *Adv. Mater.* **2005**, *17*, 2553−2559.

(14) Deng, Z.; Tian, Y.; Lee, S.-H.; Ribbe, A. E.; Mao, C. DNA-Encoded Self-Assembly of Gold Nanoparticles into One-Dimensional Arrays. *Angew. Chem., Int. Ed.* **2005**, *117*, 3648−3651.

(15) Liu, L.; Wang, T.; Li, J.; Guo, Z.-X.; Dai, L.; Zhang, D.; Zhu, D. Self-Assembly of Gold Nanoparticles to Carbon Nanotubes Using a Thiol-Terminated Pyrene as Interlinker. *Chem. Phys. Lett.* **2003**, *367*, 747−752.

(16) Grzelczak, M.; Vermant, J.; Furst, E. M.; Liz-Marzán, L. M. Directed Self-Assembly of Nanoparticles. *ACS Nano* **2010**, *4*, 3591−3605.

(17) Nie, Z.; Fava, D.; Kumacheva, E.; Zou, S.; Walker, G. C.; Rubinstein, M. Self-Assembly of Metal-Polymer Analogues of Amphiphilic Triblock Copolymers. *Nat. Mater.* **2007**, *6*, 609−614.

(18) Sun, Z.; Ni, W.; Yang, Z.; Kou, X.; Li, L.; Wang, J. pH-Controlled Reversible Assembly and Disassembly of Gold Nanorods. *Small* **2008**, *4*, 1287−1292.

(19) Feng, J.-J.; Guo, H.; Li, Y.-F.; Wang, Y.-H.; Chen, W.-Y.; Wang, A.-J. Single Molecular Functionalized Gold Nanoparticles for Hydrogen-Bonding Recognition and Colorimetric Detection of Dopamine with High Sensitivity and Selectivity. *ACS Appl. Mater. Interfaces* **2013**, *5*, 1226−1231.

(20) Lim, S.; Song, J. E.; La, J. A.; Cho, E. C. Gold Nanospheres Assembled on Hydrogel Colloids Display a Wide Range of Thermoreversible Changes in Optical Bandwidth for Various Plasmonic-Based Color Switches. *Chem. Mater.* **2014**, *26*, 3272−3279.

(21) Karg, M.; Lu, Y.; Carbó-Argibay, E.; Pastoriza-Santos, I.; Pérez-Juste, J.; Liz-Marzán, L. M.; Hellweg, T. Multiresponsive Hybrid Colloids Based on Gold Nanorods and Poly(NIPAM-co-allylacetic acid) Microgels: Temperature- and pH-Tunable Plasmon Resonance. *Langmuir* **2009**, *25*, 3163−3167.

(22) Zhang, M.; Rabiah, N. I.; Ngo, T. H.; Otanicar, T. P.; Phelan, P. E.; Swaminathan, R.; Dai, L. L. Thermo-Responsiveness and Tunable

Optical Properties of Asymmetric Polystyrene/PNIPAM-Gold Composite Particles. *J. Colloid Interface Sci.* **2014**, *425*, 12−19.

(23) Wu, Y.; Zhou, F.; Yang, L.; Liu, J. A Shrinking Strategy for Creating Dynamic SERS Hot Spots on the Surface of Thermosensitive Polymer Nanospheres. *Chem. Commun.* **2013**, *49*, 5025−5027.

(24) Huang, Z.; Meng, G.; Huang, Q.; Chen, B.; Zhou, F.; Hu, X.; Qian, Y.; Tang, H.; Han, F.; Chu, Z. Polyacrylic Acid Sodium Salt Film Entrapped Ag-Nanocubes as Molecule Traps for SERS Detection. *Nano Res.* **2014**, *7*, 1177−1187.

(25) Manikas, A. C.; Romeo, G.; Papa, A.; Netti, P. A. Highly Efficient Surface-Enhanced Raman Scattering Substrate Formulation by Self-Assembled Gold Nanoparticles Physisorbed on Poly(*N*-isopropylacrylamide) Thermoresponsive Hydrogels. *Langmuir* **2014**, *30*, 3869−3875.

(26) Karg, M.; Pastoriza-Santos, I.; Pérez-Juste, J.; Hellweg, T.; Liz-Marzán, L. M. Nanorod-Coated PNIPAM Microgels: Thermoresponsive Optical Properties. *Small* **2007**, *3*, 1222−1229.

(27) Meyerbröker, N.; Kriesche, T.; Zharnikov, M. Novel Ultrathin Poly(ethylene glycol) Films as Flexible Platform for Biological Applications and Plasmonics. *ACS Appl. Mater. Interfaces* **2013**, *5*, 2641−2649.

(28) Contreras-Caceres, R.; Dawson, C.; Formanek, P.; Fischer, D.; Simon, F.; Janke, A.; Uhlmann, P.; Stamm, M. Polymers as Templates for Au and Au@Ag Bimetallic Nanorods: UV-Vis and Surface Enhanced Raman Spectroscopy. *Chem. Mater.* **2013**, *25*, 158−169.

(29) Park, S. Y.; Lytton-Jean, A. K. R.; Lee, B.; Weigand, S.; Schatz, G. C.; Mirkin, C. A. DNA-Programmable Nanoparticle Crystallization. *Nature* **2008**, *451*, 553−556.

(30) Dan, B.; Wingfield, T. B.; Evans, J. S.; Mirri, F.; Pint, C. L.; Pasquali, M.; Smalyukh, I. I. Templating of Self-Alignment Patterns of Anisotropic Gold Nanoparticles on Ordered SWNT Macrostructures. *ACS Appl. Mater. Interfaces* **2011**, *3*, 3718−3724.

(31) Lee, Y. H.; Polavarapu, L.; Gao, N.; Yuan, P.; Xu, Q. H. Enhanced Optical Properties of Graphene Oxide−Au Nanocrystal Composites. *Langmuir* **2011**, *28*, 321−326.

(32) Guo, Y.; Zhang, Y.; Shao, H.; Wang, Z.; Wang, X.; Jiang, X. Label-Free Colorimetric Detection of Cadmium Ions in Rice Samples Using Gold Nanoparticles. *Anal. Chem.* **2014**, *86*, 8530−8534.

(33) Han, X.; Goebl, J.; Lu, Z.; Yin, Y. Role of Salt in the Spontaneous Assembly of Charged Gold Nanoparticles in Ethanol. *Langmuir* **2011**, *27*, 5282−5289.

(34) Norsten, T. B.; Frankamp, B. L.; Rotello, V. M. Metal Directed Assembly of Terpyridine-Functionalized Gold Nanoparticles. *Nano Lett.* **2002**, *2*, 1345−1348.

(35) Manikas, A. C.; Causa, F.; Della Moglie, R.; Netti, P. A. Tuning Gold Nanoparticles Interfaces by Specific Peptide Interaction for Surface Enhanced Raman Spectroscopy (SERS) and Separation Applications. *ACS Appl. Mater. Interfaces* **2013**, *5*, 7915−7922.

(36) Placido, T.; Aragay, G.; Pons, J.; Comparelli, R.; Curri, M. L.; Merkoçi, A. Ion-Directed Assembly of Gold Nanorods: A Strategy for Mercury Detection. *ACS Appl. Mater. Interfaces* **2013**, *5*, 1084−1092.

(37) Li, H.; Liu, X.; Huang, N.; Ren, K.; Jin, Q.; Ji, J. Mixed-Charge Self-Assembled Monolayers" as A Facile Method to Design pH-induced Aggregation of Large Gold Nanoparticles for Near-Infrared Photothermal Cancer Therapy. *ACS Appl. Mater. Interfaces* **2014**, *6*, 18930−18937.

(38) Ma, W.; Kuang, H.; Xu, L.; Ding, L.; Xu, C.; Wang, L.; Kotov, N. A. Attomolar DNA Detection with Chiral Nanorod Assemblies. *Nat. Commun.* **2013**, *4*, 2689.

(39) Shi, S.; Wang, Q.; Wang, T.; Ren, S.; Gao, Y.; Wang, N. Thermo-, pH-, and Light-Responsive Poly(*N*-isopropylacrylamide-*co*-methacrylic acid)−Au Hybrid Microgels Prepared by the in Situ Reduction Method Based on Au-Thiol Chemistry. *J. Phys. Chem. B* **2014**, *118*, 7177−7186.

(40) Budhlall, B. M.; Marquez, M.; Velev, O. D. Microwave, Photo- and Thermally Responsive PNIPAm−Gold Nanoparticle Microgels. *Langmuir* **2008**, *24*, 11959−11966.

(41) Nikoobakht, B.; El-Sayed, M. A. Preparation and Growth Mechanism of Gold Nanorods (NRs) Using Seed-Mediated Growth Method. *Chem. Mater.* **2003**, *15*, 1957−1962.

(42) Zhou, N.; Polavarapu, L.; Gao, N.; Pan, Y.; Yuan, P.; Wang, Q.; Xu, Q. H. TiO$_2$ Coated Au/Ag Nanorods with Enhanced Photocatalytic Activity Under Visible Light Irradiation. *Nanoscale* **2013**, *5*, 4236−4241.

(43) Bastús, N. G.; Comenge, J.; Puntes, V. C. Kinetically Controlled Seeded Growth Synthesis of Citrate-Stabilized Gold Nanoparticles of up to 200 nm: Size Focusing versus Ostwald Ripening. *Langmuir* **2011**, *27*, 11098−11105.

(44) Le Ru, E. C.; Blackie, E.; Meyer, M.; Etchegoin, P. G. Surface Enhanced Raman Scattering Enhancement Factors: A Comprehensive Study. *J. Phys. Chem. C* **2007**, *111*, 13794−13803.

(45) Ameer, F. S.; Pittman, C. U.; Zhang, D. Quantification of Resonance Raman Enhancement Factors for Rhodamine 6G (R6G) in Water and on Gold and Silver Nanoparticles: Implications for Single-Molecule R6G SERS. *J. Phys. Chem. C* **2013**, *117*, 27096−27104.

(46) Solís, D. M.; Taboada, J. M.; Obelleiro, F.; Liz-Marzán, L. M.; García de Abajo, F. J. Toward Ultimate Nanoplasmonics Modeling. *ACS Nano* **2014**, *8*, 7559−7570.

(47) Taboada, J. M.; Araujo, M. G.; Basteiro, F. O.; Rodriguez, J. L. MLFMA-FFT Parallel Algorithm for the Solution of Large-Scale Problems in Electromagnetics. *Proc. IEEE* **2013**, *101*, 350−363.

(48) Palik, E. D. *Handbook of Optical Constants of Solids*; Academic Press: New York, 1995; Vol. 1.

(49) Garner, B. W.; Cai, T.; Ghosh, S.; Hu, Z. B.; Neogi, A. Refractive Index Change Due to Volume-Phase Transition in Polyacrylamide Gel Nanospheres for Optoelectronics and Biophotanics. *Appl. Phys. Express* **2009**, *2*, 057001.

(50) Correa-Duarte, M. A.; Perez-Juste, J.; Sanchez-Iglesias, A.; Giersig, M.; Liz-Marzan, L. M. Aligning Au Nanorods by Using Carbon Nanotubes as Templates. *Angew. Chem., Int. Ed.* **2005**, *44*, 4375−4378.

(51) Harrington, R. F. *Field Computation by Moment Methods*; Wiley-IEEE Press: New York, 1993; Vol. 1.

(52) Araújo, M. G.; Taboada, J. M.; Rivero, J.; Solís, D. M.; Obelleiro, F. Solution of large-Scale Plasmonic Problems with the Multilevel Fast Multipole Algorithm. *Opt. Lett.* **2012**, *37*, 416−418.

(53) Jiming, S.; Cai-Cheng, L.; Weng Cho, C. Multilevel Fast Multipole Algorithm for Electromagnetic Scattering by Large Complex Objects. *IEEE Trans. Antennas Propag.* **1997**, *45*, 1488−1493.

(54) Álvarez-Puebla, R. A. Effects of the Excitation Wavelength on the SERS Spectrum. *J. Phys. Chem. Lett.* **2012**, *3*, 857−866.

(55) McFarland, A. D.; Young, M. A.; Dieringer, J. A.; Van Duyne, R. P. Wavelength-Scanned Surface-Enhanced Raman Excitation Spectroscopy. *J. Phys. Chem. B* **2005**, *109*, 11279−11285.

(56) Ye, J.; Hutchison, J. A.; Uji-i, H.; Hofkens, J.; Lagae, L.; Maes, G.; Borghs, G.; Van Dorpe, P. Excitation Wavelength Dependent Surface Enhanced Raman Scattering of 4-Aminothiophenol on Gold Nanorings. *Nanoscale* **2012**, *4*, 1606−1611.

(57) Samal, A. K.; Polavarapu, L.; Rodal-Cedeira, S.; Liz-Marzán, L. M.; Pérez-Juste, J.; Pastoriza-Santos, I. Size Tunable Au@Ag Core−Shell Nanoparticles: Synthesis and Surface-Enhanced Raman Scattering Properties. *Langmuir* **2013**, *29*, 15076−15082.

(58) Polavarapu, L.; Porta, A. L.; Novikov, S. M.; Coronado-Puchau, M.; Liz-Marzán, L. M. Pen-on-Paper Approach Toward the Design of Universal Surface Enhanced Raman Scattering Substrates. *Small* **2014**, *10*, 3065−3071.

(59) Kaminska, A.; Dziecielewski, I.; Weyher, J. L.; Waluk, J.; Gawinkowski, S.; Sashuk, V.; Fialkowski, M.; Sawicka, M.; Suski, T.; Porowski, S.; Holyst, R. Highly reproducible, Stable and Multiply Regenerated Surface-Enhanced Raman Scattering Substrate for Biomedical Applications. *J. Mater. Chem.* **2011**, *21*, 8662−8669.

(60) Moskovits, M. Persistent Misconceptions Regarding SERS. *Phys. Chem. Chem. Phys.* **2013**, *15*, 5301−5311.